# A Novel Multi-Objective Finite Control Set Model Predictive Control for IPMSM drive fed by a Five-Level Cascaded H-Bridge Inverter

G. Scaglione, C. Nevoloso, G. Schettino, A. O. Di Tommaso, and R. Miceli, *Member IEEE*

***Abstract*—In this work, a novel multi-objective voltage-vector-based finite control set model predictive control for a permanent magnet synchronous machine drive fed by a three-phase five-level cascaded H-bridge multilevel inverter is proposed. This algorithm aims to overcome the main issues relative to model predictive control implementation detected in the scientific literature for electric drives fed by cascaded H-bridge multilevel inverters. In detail, the goals are the minimization of computational cost by reducing the number of required predictions, the minimization of the switching devices state transitions, i.e. the switching losses minimization, and the common mode voltage reduction. These goals are fulfilled through an offline optimization process, thus, no additional terms and weighting factors to be tuned are required for the cost function. Experimental validations are presented to prove the effectiveness of the proposed approach. In detail, an accurate electric drive performance comparison, both in steady state and dynamic working conditions, is carried out when the proposed voltage-vector-based model predictive control and the cell-by-cell-based model predictive control are adopted. As comparison tools, current and voltage total harmonic distortion, apparent switching frequency, common mode voltage amplitude, and torque ripple are adopted.**

***Index Terms*—CHBMI, Electrical Drives, Model Predictive Control, FCS-MPC, IPMSM.**

## I. INTRODUCTION

Cascaded H-Bridge Multilevel Inverter (CHBMI) represents one of the most interesting Multilevel Inverter (MI) topologies, due to its modularity, scalability, lower number of required switching devices, with respect to other MI topologies, and fault-tolerant capability [1]-[2]. CHBMI has been widely adopted in high-voltage high-power grid-connected applications as Static Compensator (STATCOM) or Power Flow Controller (PFC)[3]. However, it has aroused considerable interest also in the field of medium-voltage industrial electrical drives, since it results to be the most efficient MI topology in the range of 4.16-13.8 kV, regardless of the switching devices technology [4]-[5]. Moreover, CHBMI represents an interesting solution for the e-mobility sector [6]. In detail, it allows for easy integration with the battery pack and an increment of total DC link voltage without increasing the switching devices voltage stress [7]-[8].

In order to maximize the performance of these systems in terms of power losses and control flexibility, the scientific literature efforts focus on new control software solutions such as the Model Predictive Control (MPC). MPC is a control strategy which is gaining considerable interest in the last ten years, thanks to a strong technological advancement in the field of microelectronics, which led to an increment in the controllers computational capability [9]. In detail, the Finite Control Set (FCS) MPC allows for obtaining the optimal control action by solving a state-space model-based Integer Quadratic Optimal Control Problem (IQOCP) over a prediction horizon [10]-[11]. The control objectives are synthesized into a cost function, which allows for fulfilling several conflicting goals. The adoption of the controlled system state space model allows for considering system non-linearities, which are typically correlated to converter switching behaviour in power electronics and electrical drive fields.

It's a challenging task solving the IQOCP into a sampling interval $T_s$ when MI is adopted, due to the higher number of provided Voltage Vectors (VVs) with respect to traditional Two-Level Voltage Source Inverters (2L-VSIs), i.e., the future system state must be predicted several times depending on the number of available VVs. Moreover, when CHBMI is adopted, VVs and Gate Control Signals (GCSs) sets redundancies entail a further increase of the control complexity. Several strategies

Manuscript received Day Month Year; revised Day Month Year; accepted Day Month Year. Date of publication Day Month Year; date of current version Day Month Year.

This work was supported in part by the Prin 2017-Settore/Ambito di intervento-PE7 linea C Advanced power-trains and -systems for full electric aircrafts under Grant 2017MS9F49, in part by the European Union—NextGenerationEU-National Sustainable Mobility Center CN00000023, Italian Ministry of University and Research Decree n. 1033—17/06/2022, Spoke 3, 12, CUP B73C22000760001, in part by the Prin 2022- Settore/Ambito di intervento: PE7 Enhanced Energy-Saving Powertrains for Freight E-Transportation (ESPFET) PRJ-0962-CUP B53D23002440006, in part by the Sustainable Development and Energy Saving Laboratory (SDESLAB), Laboratory of Electrical Applications (LEAP), Electrical Drive Applications Laboratory (EDALAB), Department of Engineering, University of Palermo, Italy.

Recommended for publication by Associate Editor Yam Siwakoti. (Corresponding author: Claudio Nevoloso).

Gioacchino Scaglione, Claudio Nevoloso, Giuseppe Schettino Antonino Oscar Di Tommaso and Rosario Miceli are with the Department of Engineering, University of Palermo, 90128 Palermo, Italy (e-mail: claudio.nevoloso@unipa.it).

Color versions of one or more of the figures in this article are available online at http://ieeexplore.ieee.org

have been proposed in the literature to reduce the MPC computational complexity for CHBMI-fed systems. In [12], a Cell-Cy-Cell-Based (CBCB) FCS-MPC for a Cascaded H-Bridge Rectifier (CHBR) is proposed. In detail, per each H-Bridge (HB) phase module, the IQOCP is independently formulated and solved. In [13], a hierarchical FCS-MPC is proposed for a grid-connected single-phase CHBMI. In detail, the candidate GCSs set is selected over a subregion of a 2-D control plane. The control plane allows for the candidate switching state set preselection and additional cost function terms can be deleted. In [14], an FCS-MPC for a CHBR with available VV set online variation is formulated. The VVs set is defined depending on the system working conditions (i.e., transients or stationary conditions, faults conditions, and asymmetric loads). In [15], the FCS-MPC computational growth reduction from exponential form to polynomial form is addressed by the authors. In detail, the IQOCP is split into two suboptimization problems, which deal with the current control and the optimal GCSs set selection, respectively. In [16], the same authors improved the previous algorithm with a simplified Branch and Bound (BnB) approach. In [17] Modulated Model Predictive Control ($M^2PC$) for a CHB-based synchronous compensator is proposed with voltage self-balancing ability.

In [18], a fascinating FCS-MPC with reduced available VVs candidates is proposed: in detail, the VVs candidate set at the current instant is composed of adjacent VVs to the previous optimal VV. Redundant VVs are eliminated to minimize the Common Mode Voltage (CMV) which is a prominent feature in electrical drive applications since high CMV produces bearing currents that determine an early degradation of the bearing and the winding insulation [19]. Several researchers faced the problem by adopting the MPC due to its capability to fulfill different conflicting control goals [20]. In [21] and [22], authors propose FCS-MPC-based strategies for CMV minimization in traditional 2L-VSI-based electrical drives: in detail, to avoid the use of Zero Voltage Vectors (ZVV), which determine the highest CMVs, some adjacent and nonadjacent VVs are applied for a specific time duration over a sampling period, to guarantee the lowest voltage ripple. Nevertheless, the application of non-adjacent VVs causes high voltage *dv/dt*, which are correlated to the switching devices voltage stress and electromagnetic interferences. In [23] MPC is adopted for CMV suppression for a Linear Permanent Magnet Synchronous Motor (LPMSM) drive fed by a Neutral Point Clamped Inverter (NPCI) where redundant VVs with higher CMVs are discarded. In [24] authors exploit the FCS-MPC to dynamically adjust the number of candidate vectors according to the predicted current ripple. In detail, it emerges that the ZVV must be used only in the low-speed range.

Looking at the scientific literature, the following considerations must be highlighted:

- The majority of the works in the literature that deal with FCS-MPC with CHBMI are designed for grid-connected applications where it usually operates as a rectifier. Moreover, most of the discussed control strategies require additional computation stages to evaluate the current system state, to define the VVs candidate set online, and its application time duration;
- Most of the papers that deal with CMV minimization take into account traditional 2L-VSIs, additional terms are introduced into the cost function and this makes the weighing factor tuning an annoying activity;
- Looking at [18], although both the computational cost reduction and CMV minimization goals are fulfilled, several issues are left unanswered: CHBMI exhibits not only VVs but also GCSs redundancy, i.e., the same phase voltage set can be synthesized by several switching state combinations; managing GCSs redundancies is a challenging task. Moreover, the FCS-MPC has been designed on a passive RL load, and its impact on an electrical drive is missing. The practical algorithm implementation is not discussed.

This work aims to overcome the main weaknesses of the control strategy presented in [18] by designing and implementing a novel Multi-Objective Voltage-Vector-Based (VVB) FCS-MPC for PMSM drives fed by CHBMI. In detail, the control must fulfill the following goals: computational burden minimization, CMVs minimization, GCS transitions minimization, and phase voltages *dv/dt* minimization. It must be underlined that the control optimization process is carried out offline, to reduce the online computation amount and, once it is completed, the proposed goals are automatically fulfilled, i.e., no additional cost function terms are required, unlike other proposed FCS-MPCs in the literature. This feature allows for avoiding the weighting factors tuning process, which is an annoying activity when the cost function is composed of many terms. The offline optimization process deals with the redundant VVs with high CMVs elimination and optimal GCS set selection, to minimize the switching devices state transitions. An online selection algorithm is implemented to predict the future system state only with respect to the adjacent VVs to the currently applied one. This constraint allows for minimizing both the optimal control problem computational burden since only seven predictions must be carried out at each sampling period and minimizing the voltage *dv/dt* since phase voltage instantaneous excursion is limited to one HB DC link voltage.

For experimental validation purposes, a test bench with an Interior Permanent Magnet Synchronous Motor (IPMSM) drive fed by a Three-Phase Five-Level (3P-5L) CHBMI has been set up. Experimental tests are carried out to verify the proposed control effectiveness: in detail, the electric drive performance, both in steady state and dynamic working condition, are analyzed and compared when the proposed VVB-FCS and the CBCB-MPC presented in [12] are adopted. It must be underlined that the algorithm presented in [12] has been chosen as the comparison target for the following reasons: firstly, the CBCB approach allows for reducing the control computational complexity by introducing some specific switching constraints that exploit the CHB topology; this constraints-based control design approach is homogeneous with the one adopted in this work; moreover, no BnB approach must be adopted to solve the

optimal control problem and this makes the control implementation quite easy; last but not least, although the CBCB algorithm is proposed for a single-phase CHB rectifier, its strong correlation with the converter topology allows to easily adapt the algorithm to a three-phase electric drive application. All these features make the CBCB algorithm a direct competitor of the VVB MPC. As comparison tools, current and voltage total harmonic distortion, apparent switching frequency, common mode voltage amplitude, and torque ripple are adopted.

This work is organized as follows: Section II describes the FCS-MPC mathematical formulation; Section III presents the proposed algorithm; Section IV describes the test bench; Section V presents and analyzes the experimental results. Finally, section VI summarizes the work results.

## II. Model Predictive Control Formulation

In this section, the IQOCP is formulated. In detail, both IPMSM and the 3P-5L CHBMI control models are introduced. The electric drive control scheme is reported in Fig.1.

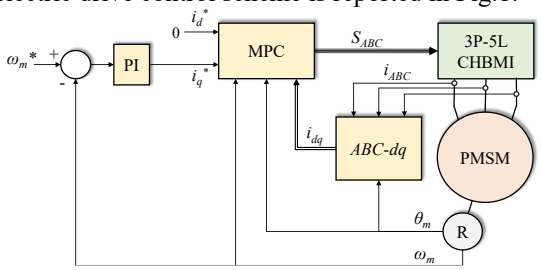


**Fig. 1.** Electric drive with FCS-MPC control block scheme.

In detail, motor speed and currents are chosen as controlled variables. The outer control loop allows generating the current references in the *d-q* reference frame, for this purpose PI controller is adopted. The inner control loop is synthesized as an FCS-MPC.

### *A. IPMSM control model*

For control formulation purposes, the IPMSM continuous-time state-space model in the two-phase *d-q* reference frame is considered:

$$\frac{d}{dt}\boldsymbol{i}_{dq}(t) = \boldsymbol{F}\boldsymbol{i}_{dq}(t) + \boldsymbol{G}\boldsymbol{v}_{dq}(t) + \boldsymbol{H} \tag{1}$$

with

$$\boldsymbol{F} = \begin{bmatrix} -\frac{R}{L_d} & \frac{p\omega_m L_q}{L_d} \\ -\frac{p\omega_m L_d}{L_q} & -\frac{R}{L_q} \end{bmatrix}, \boldsymbol{G} = \begin{bmatrix} \frac{1}{L_d} & 0 \\ 0 & \frac{1}{L_q} \end{bmatrix}, \boldsymbol{H} = \begin{bmatrix} 0 \\ -\frac{p\omega_m \lambda_{PM}}{L_q} \end{bmatrix}, \tag{2}$$

where $\boldsymbol{v}_{dq}$, is the stator voltage vector, $\boldsymbol{i}_{dq}$, is the stator current vector, $L_d$, $L_q$ are direct and quadrature inductances, $R$ is the stator winding resistance, $\omega_m$ is the mechanical rotor speed, $\lambda_{PM}$ is the permanent magnet flux linkage and $p$ is the pole pairs of the machine. By discretizing equations (1) with forward-Euler approximation, the discrete-time state-space model is obtained:

$$\boldsymbol{i}_{dq}(k+1) = \boldsymbol{A}\boldsymbol{i}_{dq}(k) + \boldsymbol{B}\boldsymbol{v}_{dq}(k) + \boldsymbol{K} \tag{3}$$

with

$$\boldsymbol{A} = \begin{bmatrix} 1-\frac{T_s R}{L_d} & \frac{p\omega_m T_s L_q}{L_d} \\ -\frac{p\omega_m T_s L_d}{L_q} & 1-\frac{T_s R}{L_q} \end{bmatrix} \boldsymbol{B} = \begin{bmatrix} \frac{T_s}{L_d} & 0 \\ 0 & \frac{T_s}{L_q} \end{bmatrix}, \boldsymbol{K} = \begin{bmatrix} 0 \\ -\frac{p\omega_m T_s \lambda_{PM}}{L_q} \end{bmatrix}, \tag{4}$$

### *B. CHBMI control model*

The control model of the 3P-5L CHBMI, whose circuit diagram is reported in Fig.2, must be defined, and integrated with the motor model.

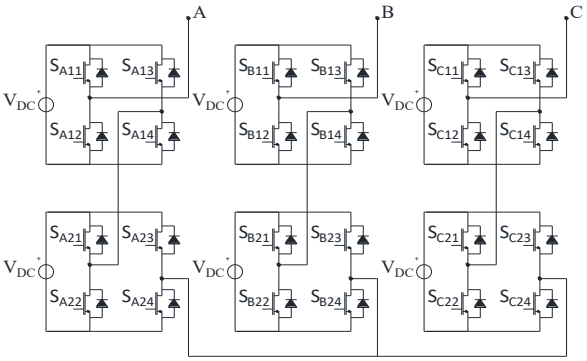


**Fig. 2.** Three-phase five-level CHBMI circuit diagram.

With this aim, the input voltage vector $\boldsymbol{v}_{dq}$ must be expressed regarding the converter switching states. In detail, with respect to the circuit diagram reported in Fig.2, and taking into account that, in order to avoid leg short circuit, switching devices on the same HB leg must work in a complementary way, the phase voltage can be expressed as:

$$v_{jN} = v_{DC}(S_{j,11} - S_{j,13} + S_{j,21} - S_{j,23}), \tag{5}$$

where $v_{DC}$ is the HB DC-link voltage and $S_{j,xy}$ is the HB leg state variable, $j \in \{A, B, C\}$ identifies the converter phase, $x \in \{1, 2\}$ identifies the HB phase module, and $y \in \{1, 4\}$ identifies the HB leg. Phase voltage vectors in *d-q* reference frame and *ABC* reference frame are linked by the relation:

$$\boldsymbol{v}_{dq}(t) = \boldsymbol{T}\boldsymbol{v}_N(t) \tag{6}$$

with

$$\boldsymbol{T} = \frac{2}{3}\begin{bmatrix} \cos(p\theta) & \cos\left(p\theta - \frac{2\pi}{3}\right) & \cos\left(p\theta + \frac{2\pi}{3}\right) \\ -\sin(p\theta) & -\sin\left(p\theta - \frac{2\pi}{3}\right) & -\sin\left(p\theta + \frac{2\pi}{3}\right) \end{bmatrix} \tag{7}$$

where $\theta$ is the rotor angular position.

### *C. Cost function*

A prediction horizon $N_p$=1 is chosen and the cost function $J$ is formulated as:

$$J = \left\| \boldsymbol{i}_{dq}^*(k+1) - \boldsymbol{i}_{dq}(k+1) \right\|_2^2 \tag{8}$$

where $\boldsymbol{i}_{dq}^*$ is the reference currents vector, $\boldsymbol{i}_{dq}$ is the future state current vector. The cost function penalizes the input current error only.

## III. Voltage Vectors-Based Optimization Process

In this section, the adopted strategy to simplify the IQOCP resolution is discussed. In detail, the offline optimization process and the simplified control algorithm implementation are discussed.

### *A. Offline Optimization process*

In Fig. 3, the VVs of a 3P-5L-CHBMI in the *α-β* reference frame are represented. In order to minimize the computational burden, the number of predictions must be minimized. With this aim, the set of available VVs at the $k_{th}$ sampling period consists only of the adjacent VVs to the currently applied one. As a way of example, with respect to Fig. 3, at the $k_{th}$ sampling period, the applied voltage vector is $v_{16}$, which is identified by the red circle.

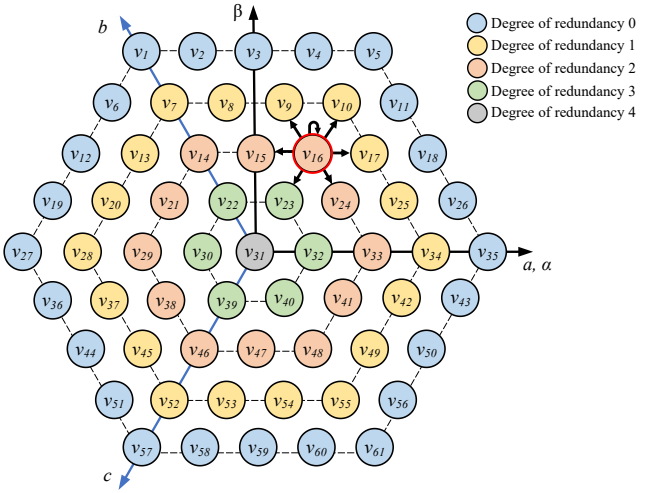


**Fig. 3.** Voltage vectors on the *α-β* plane.

At the $k+1_{th}$ sampling instant, the system can move to the adjacent vectors $v_{17}$, $v_{24}$, $v_{23}$, $v_{15}$, $v_9$, and $v_{10}$ or remain in $v_{16}$. In general, the number of available VVs to be tested in a sampling interval is equal to 7 (i.e., 6 adjacent vectors and the currently applied vector itself), except when the current vector belongs to the outer hexagon; in this case, the number of available input variable sets is equal to 4 when the current vector lies on one of the six edges of the hexagon, and 5 in other cases. The total number of VVs in the *α-β* reference frame is obtained as follows:

$$N_{v,\alpha\beta} = n_l^m = 5^3 = 125 \tag{9}$$

where $n_l$ is the number of phase voltage levels and $m$ is the number of phases. Looking at Fig. 3, it can be noted that most of the 125 VVs are superimposed, which means that most of the VVs are redundant. In detail, by identifying four concentric hexagons and by moving from the outer to the inner one, the degree of redundancy assigned to the VVs which lie on each hexagon goes from 0 (i.e., no redundant VVs) to 3. The ZVV has a degree of redundancy equal to 4. In order to minimize the CMVs, per each VV, the Phase Voltages Combinations (PVCs) which minimized the CMV are saved and other combinations are discarded. CMVs are computed according to the following relation:

$$v_{cm} = \frac{v_{aN} + v_{bN} + v_{cN}}{3}. \tag{10}$$

As a way of example, the vector $v_7$ is considered: it can be obtained by the following PVCs, expressed in the sequence of the phases *A B C* and in per unit (p.u.) with respect to the voltage $v_{DC}$: (-1 2 -1) and (-2 1 -2). These PVCs generate CMVs, expressed in p.u., of 0 V and -1 V respectively. In this case, the PVC is saved and the last is discarded. About vector $v_{14}$, it can be obtained by the PVCs (0 2 0), (-1 1 -1), and (-2 0 -2) which generate CMVs of 2/3 V, -1/3 V and -4/3 V respectively. In this case, the PVC (-1 1 -1) is saved and the others are discarded.

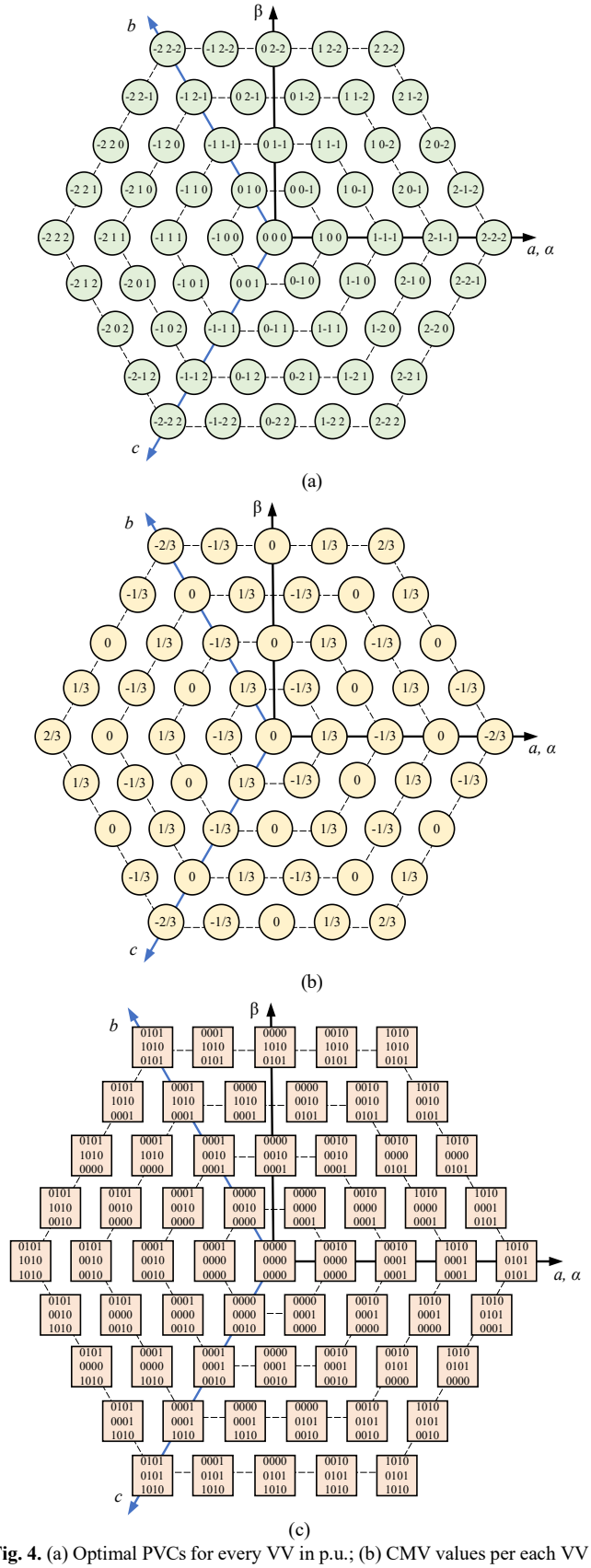


**Fig. 4.** (a) Optimal PVCs for every VV in p.u.; (b) CMV values per each VV in p.u., (c) GCSs which minimize the switching transitions, reported on the *α-β* plane.

TABLE I
TRANSITION $V_1$ ➔ $V_6$

| | $S_{A11}$ | $S_{A13}$ | $S_{A21}$ | $S_{A23}$ | $S_{B11}$ | $S_{B13}$ | $S_{B21}$ | $S_{B23}$ | $S_{C11}$ | $S_{C13}$ | $S_{C21}$ | $S_{C23}$ | Number of GCSs transitions |
|---|---|---|---|---|---|---|---|---|---|---|---|---|---|
| $v_1$ | 0 | 1 | 0 | 1 | 1 | 0 | 1 | 0 | 0 | 1 | 0 | 1 | |
| $v_6$ | 0 | 1 | 0 | 1 | 1 | 0 | 1 | 0 | 0 | 0 | 0 | 1 | 1 |
| | 0 | 1 | 0 | 1 | 1 | 0 | 1 | 0 | 0 | 1 | 0 | 0 | 1 |
| | 0 | 1 | 0 | 1 | 1 | 0 | 1 | 0 | 0 | 1 | 1 | 1 | 1 |
| | 0 | 1 | 0 | 1 | 1 | 0 | 1 | 0 | 1 | 1 | 0 | 1 | 1 |

TABLE II
TRANSITION $V_1$ ➔ $V_7$

| | $S_{A11}$ | $S_{A13}$ | $S_{A21}$ | $S_{A23}$ | $S_{B11}$ | $S_{B13}$ | $S_{B21}$ | $S_{B23}$ | $S_{C11}$ | $S_{C13}$ | $S_{C21}$ | $S_{C23}$ | Number of transitions |
|---|---|---|---|---|---|---|---|---|---|---|---|---|---|
| $v_1$ | 0 | 1 | 0 | 1 | 1 | 0 | 1 | 0 | 0 | 1 | 0 | 1 | |
| $v_7$ | 0 | 0 | 0 | 1 | 1 | 0 | 1 | 0 | 0 | 0 | 0 | 1 | 2 |
| | 0 | 0 | 0 | 1 | 1 | 0 | 1 | 0 | 0 | 1 | 0 | 0 | 2 |
| | 0 | 0 | 0 | 1 | 1 | 0 | 1 | 0 | 0 | 1 | 1 | 1 | 2 |
| | 0 | 0 | 0 | 1 | 1 | 0 | 1 | 0 | 1 | 1 | 0 | 1 | 2 |
| | 0 | 1 | 0 | 0 | 1 | 0 | 1 | 0 | 0 | 0 | 0 | 1 | 2 |
| | 0 | 1 | 0 | 0 | 1 | 0 | 1 | 0 | 0 | 1 | 0 | 0 | 2 |
| | 0 | 1 | 0 | 0 | 1 | 0 | 1 | 0 | 0 | 1 | 1 | 1 | 2 |
| | 0 | 1 | 0 | 0 | 1 | 0 | 1 | 0 | 1 | 1 | 0 | 1 | 2 |
| | 0 | 1 | 1 | 1 | 1 | 0 | 1 | 0 | 0 | 0 | 0 | 1 | 2 |
| | 0 | 1 | 1 | 1 | 1 | 0 | 1 | 0 | 0 | 1 | 0 | 0 | 2 |
| | 0 | 1 | 1 | 1 | 1 | 0 | 1 | 0 | 0 | 1 | 1 | 1 | 2 |
| | 0 | 1 | 1 | 1 | 1 | 0 | 1 | 0 | 1 | 1 | 0 | 1 | 2 |
| | 1 | 1 | 0 | 1 | 1 | 0 | 1 | 0 | 0 | 0 | 0 | 1 | 2 |
| | 1 | 1 | 0 | 1 | 1 | 0 | 1 | 0 | 0 | 1 | 0 | 0 | 2 |
| | 1 | 1 | 0 | 1 | 1 | 0 | 1 | 0 | 0 | 1 | 1 | 1 | 2 |
| | 1 | 1 | 0 | 1 | 1 | 0 | 1 | 0 | 1 | 1 | 0 | 1 | 2 |

TABLE III
TRANSITION $V_6$ ➔ $V_7$

| | $S_{A11}$ | $S_{A13}$ | $S_{A21}$ | $S_{A23}$ | $S_{B11}$ | $S_{B13}$ | $S_{B21}$ | $S_{B23}$ | $S_{C11}$ | $S_{C13}$ | $S_{C21}$ | $S_{C23}$ | Number of GCSs transitions |
|---|---|---|---|---|---|---|---|---|---|---|---|---|---|
| $v_6$ | 0 | 1 | 0 | 1 | 1 | 0 | 1 | 0 | 0 | 0 | 0 | 1 | |
| $v_7$ | 0 | 0 | 0 | 1 | 1 | 0 | 1 | 0 | 0 | 0 | 0 | 1 | 1 |
| | 0 | 0 | 0 | 1 | 1 | 0 | 1 | 0 | 0 | 1 | 0 | 0 | 3 |
| | 0 | 0 | 0 | 1 | 1 | 0 | 1 | 0 | 0 | 1 | 1 | 1 | 3 |
| | 0 | 0 | 0 | 1 | 1 | 0 | 1 | 0 | 1 | 1 | 0 | 1 | 3 |
| | 0 | 1 | 0 | 0 | 1 | 0 | 1 | 0 | 0 | 0 | 0 | 1 | 1 |
| | 0 | 1 | 0 | 0 | 1 | 0 | 1 | 0 | 0 | 1 | 0 | 0 | 3 |
| | 0 | 1 | 0 | 0 | 1 | 0 | 1 | 0 | 0 | 1 | 1 | 1 | 3 |
| | 0 | 1 | 0 | 0 | 1 | 0 | 1 | 0 | 1 | 1 | 0 | 1 | 3 |
| | 0 | 1 | 1 | 1 | 1 | 0 | 1 | 0 | 0 | 0 | 0 | 1 | 1 |
| | 0 | 1 | 1 | 1 | 1 | 0 | 1 | 0 | 0 | 1 | 0 | 0 | 3 |
| | 0 | 1 | 1 | 1 | 1 | 0 | 1 | 0 | 0 | 1 | 1 | 1 | 3 |
| | 0 | 1 | 1 | 1 | 1 | 0 | 1 | 0 | 1 | 1 | 0 | 1 | 3 |
| | 1 | 1 | 0 | 1 | 1 | 0 | 1 | 0 | 0 | 0 | 0 | 1 | 1 |
| | 1 | 1 | 0 | 1 | 1 | 0 | 1 | 0 | 0 | 1 | 0 | 0 | 3 |
| | 1 | 1 | 0 | 1 | 1 | 0 | 1 | 0 | 0 | 1 | 1 | 1 | 3 |
| | 1 | 1 | 0 | 1 | 1 | 0 | 1 | 0 | 1 | 1 | 0 | 1 | 3 |

Going on with the remaining VVs, it can be noted that there is always only one PVC which minimizes the CMV, this makes the VVs selection very easy. In Fig. 4a and b, the PVCs which minimize the CMVs per each VV and the corresponding CMVs are reported, respectively. Now, the GCSs are considered. According to (5), the VVs can be synthetized by a number of GCSs combinations $N_{GCSs}$ expressed as:

$$N_{GCSs} = 2^{(n_l-1)m} \tag{11}$$

which is equal to 4096 when $n_l$=5 and $m$=3. Therefore, the non-redundant VVs selected in the previous step can be synthesized by several GCSs sets. In order to minimize the GCSs transitions, which are correlated with the switching losses, one optimal GCSs set must be assigned to each VV. The GCSs assignment procedure is a trial-and-error iterative process, which is briefly discussed below. Taking into account the generic state transition $v_i$➔ $v_j$ and assuming that the GCSs set $\boldsymbol{S}_i$ (expressed as a row of 12 Boolean elements) is always known since it has been assigned previously, the goal is to find the set $\boldsymbol{S}_j$ which minimizes the transition $\boldsymbol{S}_i$➔ $\boldsymbol{S}_j$, for every $v_i$ adjacent to $v_j$. As a way of example, if the VV $v_1$ is currently applied, the system can move to vectors $v_2$, $v_6$, $v_7$. Assuming that $\boldsymbol{S}_1$ is known, in Table I, the transition $v_1$➔ $v_6$ is considered: it can be noted that the number of transitions is the same and equal to 1 for every $\boldsymbol{S}_6$. Therefore, the optimal set is chosen arbitrarily (green row in Table I). The same considerations can be applied to the transition $v_1$➔ $v_7$, which is

summarized in Table II. Now, transition $v_6 \rightarrow v_7$ is considered. In detail, the goal is to verify if the previously selected sets $\boldsymbol{S}_6$ and $\boldsymbol{S}_7$ allow also minimizing transitions $v_6 \rightarrow v_7$, which is summarized in Table III. Looking at Table III, the number of transitions is equal to 1 and 3, depending on the considered GCS set. Sets that determine 3 state transitions (red rows in Table III) are discarded. Among the remaining sets, the first one (green row in Table III) coincides with the previously selected set. As can be seen, the selected sets $\boldsymbol{S}_6$ and $\boldsymbol{S}_7$ minimize also the transitions $v_6 \rightarrow v_7$. Going on with all the remaining VVs transitions, one GCS set is assigned to each VV. The optimal GCSs are reported in Fig. 4c.

Once a unique match between VVs, PVCs, and GCSs sets is found, the offline optimization process is completed. For control algorithm implementation purposes, the selected sets of PVCs and GCSs are stored into two Look-Up Tables (LUTs), called LUT-1 and LUT-2, respectively. This approach allows to easily define the set of available PVCs and relative GCSs at the sampling instant $k$, depending on the previous optimal control action, without affecting the algorithm computational cost, since the access to the elements of LUTs is instantaneous and does not require extra-computations. This aspect is remarked in Section III-B, where the algorithm implementation is discussed. The final optimal control problem is formulated as follows:

$$\boldsymbol{v}_{dq,opt} = \arg\min J\left(\boldsymbol{i}_{dq}(k+1), \boldsymbol{v}_{dq}(k)\right)$$
$$subject\ to \begin{cases} \boldsymbol{i}_{dq}(k+1) = \boldsymbol{A}\boldsymbol{i}_{dq}(k) + \boldsymbol{B}\boldsymbol{v}_{dq}(k) + \boldsymbol{K} \\ \left|\Delta v_{jN}(k)\right| \le v_{DC} \\ \boldsymbol{v}_{dq}(k) \in \boldsymbol{\mathcal{U}}(k) \end{cases} \quad (12)$$

where $\boldsymbol{\mathcal{U}}(k)$ identifies the available input variables set at the $k_{th}$ sampling instant, which depends on the VV that is currently applied to the system.

### *B. Control Algorithm Implementation*

In this section, the algorithm implementation is discussed. The proposed control algorithm is summarized in Algorithm 1. As first, operations that can be executed once per sampling period, i.e., the delay time compensation, are implemented. In detail, due to the fact that the control execution time is always higher than zero, a delay is introduced between the sampling instant and the control action application instant. Such a delay depends on the algorithm computational complexity and on the adopted controller. In this application, the control action is instantaneously applied when it is available, instead of being stored and applied to the next sampling instant, as is usual when control with a modulator is adopted. As a consequence, the delay time $T_d$ coincides with the execution time. These aspects are illustrated in Fig. 5: in detail, the ideal case with a null execution time (i.e. a delay time $T_d$=0) and the real case with a non-null execution time (i.e. a delay time $T_d \neq 0$) are reported in Fig. 5(a) and Fig.5 (b), respectively. Ignoring the delay time in practical applications can determine non-accurate future system state predictions, which lead to the application of sub-optimal solutions to the controlled system and, as a consequence, current and torque ripple [25].

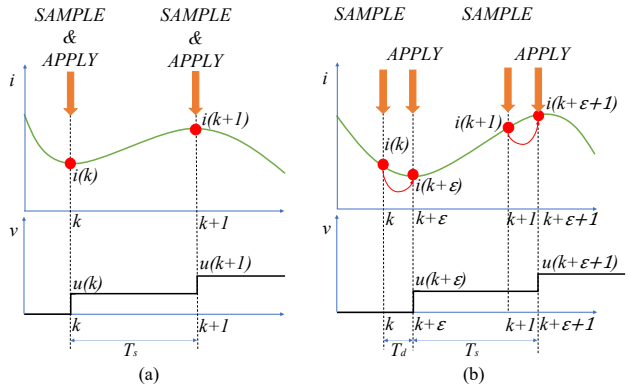


**Fig. 5.** Control actions: (a) ideal case, $T_d = 0$; (b) real case, $T_d \neq 0$.

In order to take into account such execution time, a delay compensation strategy is adopted. By assuming that the delay time $T_d$ is known and constant for each sampling period, and assuming the speed $\omega_m$ and the angular position $\theta$ constant over the sampling period, an initial prediction is performed to project the system state from instant $k$ to the instant $k+\varepsilon$, where $\varepsilon$ is the control action application instant, which is between the $k_{th}$ and $k+1_{th}$ sampling instants and is correlated with the delay time $T_d$, according to Fig. 5. The system state at the instant $k+\varepsilon$ represents the new current state to adopt for the future state predictions. The initial prediction is performed according to (13):

$$\boldsymbol{i}_{dq}(k+\varepsilon) = \boldsymbol{A}_d \boldsymbol{i}_{dq}(k) + \boldsymbol{B}_d \boldsymbol{v}_{dq,opt}(k+\varepsilon-1) + \boldsymbol{K}_d \quad (13)$$

with $\boldsymbol{A}_d$, $\boldsymbol{B}_d$, and $\boldsymbol{K}_d$ defined as in (4) but replacing the delay time $T_d$ with the sampling time $T_s$, as follows:

$$\boldsymbol{A}_d = \begin{bmatrix} 1-\frac{T_d R}{L_d} & \frac{p\omega_m T_d L_q}{L_d} \\ -\frac{p\omega_m T_d L_d}{L_q} & 1-\frac{T_d R}{L_q} \end{bmatrix} \boldsymbol{B}_d = \begin{bmatrix} \frac{T_d}{L_d} & 0 \\ 0 & \frac{T_d}{L_q} \end{bmatrix} \boldsymbol{K}_d = \begin{bmatrix} 0 \\ -\frac{p\omega_m T_d \lambda_{PM}}{L_q} \end{bmatrix} \quad (14)$$

and $\boldsymbol{v}_{dq,\,opt}$ is the optimal input vector applied to the system at the instant $k+\varepsilon-1$, which is also applied at the sampling instant $k$ and whose value is known. Once the system state at the instant $k+\varepsilon$ is estimated, it is possible to predict the state at the instant $k+\varepsilon+1$, that is, according to Fig 5, the future control action application instant, as follows:

$$\boldsymbol{i}_{dq}(k+\varepsilon+1) = \boldsymbol{A}\boldsymbol{i}_{dq}(k+\varepsilon) + \boldsymbol{B}\boldsymbol{v}_{dq}(k+\varepsilon) + \boldsymbol{K} \quad (15)$$

with matrices $\boldsymbol{A}$, $\boldsymbol{B}$, and $\boldsymbol{K}$ defined as in (4). Replacing (6) and (13) in (15) and rearranging, the following relation is obtained:

$$\boldsymbol{i}_{dq}(k+\varepsilon+1) = \boldsymbol{A}\boldsymbol{A}_d \boldsymbol{i}_{dq}(k) + \boldsymbol{A}\boldsymbol{B}_d \boldsymbol{T}\boldsymbol{v}_{N,opt}(k+\varepsilon-1) + \boldsymbol{A}\boldsymbol{K}_d + \boldsymbol{B}\boldsymbol{T}\boldsymbol{v}_N(k+\varepsilon) + \boldsymbol{K} \quad (16)$$

Looking at equation (16), it can be noted that only the term $\boldsymbol{B}\boldsymbol{v}_{dq}(k+\varepsilon)$ depends on the phase voltage vector $\boldsymbol{v}_N$. Therefore, the term $\boldsymbol{i}_{dq,p1}(k+\varepsilon+1)$ can be defined:

$$\boldsymbol{i}_{dq,p1}(k+\varepsilon+1) = \boldsymbol{A}\boldsymbol{A}_d \boldsymbol{i}_{dq}(k) + \boldsymbol{A}\boldsymbol{B}_d \boldsymbol{T}\boldsymbol{v}_{N,opt}(k+\varepsilon-1) + \boldsymbol{A}\boldsymbol{K}_d + \boldsymbol{K} \quad (17)$$

This term can be computed only once per sampling period since it is the same for all 7 predictions. Thus, expression (16) can be rewritten as:

$$\boldsymbol{i}_{dq}(k+\varepsilon+1) = \boldsymbol{i}_{dq,p1}(k+\varepsilon+1) + \boldsymbol{B}\boldsymbol{T}\boldsymbol{v}_N(k+\varepsilon) \quad (18)$$

Next, based on the currently applied VV, the set of available VVs and the corresponding PVCs are defined. This operation is carried out by acceding to a LUT: in detail, each VV is identified by a number $v_x$, according to the enumeration in Fig. 3, which represents the address to accede to the LUT, and a PVC, according to Fig. 4a. Since the currently applied VV is known, the set of available 7 VVs for future state predictions is identified. It must be underlined that this operation is extremely fast because access to LUTs doesn't affect the computational burden and the algorithm execution time. Once the 7 VVs are known, the 7 corresponding predictions are carried out. The VV which minimizes the cost function $J$ represents the solution to the IQOCP and the corresponding GCS set is identified through another LUT and applied to the system.

**Algorithm 1 Model Predictive Control**

1: **function** MPC ($\boldsymbol{i}_{dq}(k)$, $\boldsymbol{i}^*_{dq}(k)$, $\boldsymbol{S}_{opt}(k-1)$, $\omega_m(k)$, $\theta_m(k)$, $M(k-1)$)
2: Compute $\boldsymbol{i}_{dq,p1}(k+\varepsilon+1)$, according to (17)
3 Compute $\boldsymbol{BT}(k)$
4: Access to LUT1: Define the set of 7 $\boldsymbol{v}_N(k+\varepsilon)$ and $v_x$, based on $v_{x,opt}(k+\varepsilon-1)$
5: Initialize cost function $J_0$
6: **for** $y$=1: 7
7: Compute $\boldsymbol{i}_{dq}(k+\varepsilon+1, y)$ according to (18)
8: Compute $J(y)$, according to (8)
9: **if** $J(y) \leqslant J_0$
10: $J_0 \leftarrow J(y)$
11: $v_{x,opt}(k+\varepsilon) \leftarrow v_x(y)$
12: **end if**
13: **end for**
14 Access to LUT2: Define $\boldsymbol{S}_{opt}(k+\varepsilon)$, based on $v_{x,opt}(k+\varepsilon)$
15: Apply $\boldsymbol{S}_{opt}(k+\varepsilon)$ to the system
16: **end function**

### *C. Computational cost comparison with CBCB-MPC*

As discussed in the introduction of this work, the CBCB-MPC algorithm presented in [12] represents a computationally cost-effective, easy-to-implement algorithm that exploits the potentialities of the CHB topology; therefore, it becomes the best available comparison target of this work. To make the comparative analysis as fair as possible, the CBCB-MPC implementation has been carried out almost in the same way as discussed in the previous sections about the VVB-MPC: in detail, the electric drive control model, the cost function, the delay time compensation strategy, the model parameters and the sampling frequency are the same as discussed in equations (3), (4), (5), (6), (7), (8), (13) and in table V, respectively. To minimize the computational cost, also in this case the prediction equation has been split into a term that can be computed only once per sampling period and a term, which depends on the available phase voltages at the current sampling instant, which must be computed several times to carry out the future state predictions, according to equations (17) and (18). According to [12], the algorithm for the single-phase rectifier must carry out two or three predictions, depending on the current inverter state. To adapt the algorithm for a three-phase electrical drive, the phase-voltage combinations must be taken into account. Thus, the maximum number of predictions becomes $3^3$=27. To carry out these predictions, the second term of (18) is computed into three nested *for* loops, one per each phase.

The adopted controller for this application is the System on Module (SoM) sbRIO 9651, which consists of an FPGA and a DSP module and they can be programmed independently in the LabVIEW environment. The presented algorithm is entirely implemented on the FPGA target with single-precision floating point data. The Real-Time target has been adopted only for the implementation of the Graphical User Interface (GUI). In Table IV, the control parameters adopted for the CBCB-MPC and the VVB-MPC are reported: in detail, the adopted sampling period is equal to 100 µs in both cases, the computational time has been experimentally measured and it is equal to 55 µs and 23 µs for CBCB-MPC and VVB-MPC, respectively. It can be noted that CBCB-MPC requires more than twice the time needed by the VVB-MPC to elaborate the control action, due to the higher number of predictions required. In this case, the voltage-vector-based approach results in being more efficient than the phase-by-phase-based one. In Table V, the control computational resources employed for the CBCB-MPC and the VVB-MPC are reported. It must be underlined that employed computational resources and computational time deal with the whole control, which consists not only of the current control, which is synthesized as the proposed FCS-MPC but also includes the sampling process, the Angle Tracking Observer (ATO) algorithm for the speed and position measurement, the outer speed loop, which is synthesized as common PI controller. These parts of the control are deeply discussed in [26] and [27].

TABLE IV
FCS-MPC PARAMETERS

| Quantity | Symbol | Value |
|---|---|---|
| DC LinkVoltage | $V_{DC}$ | 55 V |
| Pole pairs | $p$ | 3 |
| Stator resistance | $R$ | 2.21 Ω |
| Direct inductance | $L_d$ | 0.0088 H |
| Quadrature inductance | $L_q$ | 0.0125 H |
| PM direct flux | $\lambda_{PM}$ | 0.0913 Wb |
| Sampling period | $T_s$ | 100 µs |
| Delay time CBCB-MPC | $T_d$ | 55 µs |
| Delay time VVB-MPC | $T_d$ | 23 µs |

TABLE V
EMPLOYED COMPUTATIONAL RESOURCES ON SOM SBRIO 9651.

| Device Utilization | Available resources | Employed resources [%] | |
|---|---|---|---|
| | | CBCB-MPC | VVB-MPC |
| Total slices | 13300 | 86.9 | 86.8 |
| Slice registers | 106400 | 26.7 | 26.8 |
| Slice LUTs | 53200 | 68.2 | 67.9 |
| Block RAMs | 140 | 6.4 | 7.1 |
| DSP48s | 220 | 90.9 | 88.2 |

## V. TEST BENCH

In this section, the test bench, whose picture is reported in Fig. 6, is discussed. The electrical drive consists of six MOSFET-based power H-Bridges powered by six DC power supply RSO-2400 and 6 poles three-phase BLQ - 40 IPMSM. Electrical drive technical data are summarized in Tables IV, V, and VI of [27]. A MAGTROL HD-715 hysteresis brake controlled by a MAGTROL DSP6001 high-speed programmable dynamometer is used to apply a load torque to the IPMSM. The

electrical quantities are acquired by Teledyne LeCroy MDA 8038HD oscilloscope, equipped with three high voltage differential probes Teledyne Lecroy HVD3106A 1 kV, 120 MHz, and three high sensitivity current probe Teledyne Lecroy CP030A AC/DC, 30 A rms, 50 MHz.

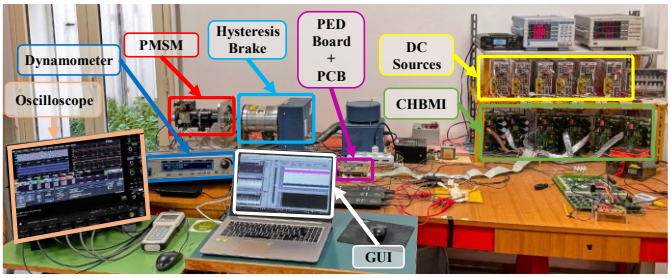


**Fig. 6.** Test bench.

## V. Experimental Results

In this section, experimental results are presented to validate the effectiveness of the proposed control algorithm. In detail, an extensive comparative analysis is carried out with the CBCB-MPC presented in [12]. For steady-state performance analysis, a set of working points (WPs) have been defined as a function of IPMSM working conditions in terms of speed $n$ and load torque $T$. The considered working points are summarized in Table VI. For each identified WP, phase voltages and phase currents are measured with Teledyne LeCroy MDA 8028HD oscilloscope, with an observation window of 1 s and a sampling frequency of 1 MS/s. To investigate the electromagnetic torque behaviour, for each identified WP, the electromagnetic torque $T_{em}$ is estimated starting by the $d$-$q$ control currents acquired. The currents are sampled with a sampling frequency of 10 kHz, which is the same adopted for the control algorithm, with an observation window of 1 s. As performance metrics, the switching frequency which is correlated to the converter switching losses, the current and voltage THD which are correlated to the copper losses and the iron losses, respectively, the common mode voltage and the torque ripple are considered.

TABLE VI
Electric Drive Working Points

| $T$ [Nm]- $n$ [rpm] | 200 | 1000 | 2000 | 3000 | 4000 |
|---|---|---|---|---|---|
| 1.8 | WP5 | WP4 | WP3 | WP2 | WP1 |
| 1.35 | WP10 | WP9 | WP8 | WP7 | WP6 |
| 0.9 | WP15 | WP14 | WP13 | WP12 | WP11 |
| 0.45 | WP20 | WP19 | WP18 | WP17 | WP16 |

With respect to the dynamic behaviour analysis, a cycle composed of a 0-3000 rpm acceleration, including no-load and rated-load operations, has been carried out. During dynamic analysis, the maximum allowed transitory currents were set to $i_q$=10 A and $i_d$ =0, respectively. IPMSM phase voltages, phase currents, load torque applied by the brake and speed signals are acquired with MDA 8028HD oscilloscope by setting an observation window of 5 s and a sampling frequency of 500 kS/s.

### *A. Steady-state condition analysis*

The phase voltages produced by the CBCB-MPC and the VVB-MPC in the time and frequency domain are reported in Fig.7 (a-j) and Fig.7 (k-u), respectively, when the load torque is fixed equal to 1.8 Nm and the speed is varied over the defined working range. Concerning the VVB-MPC, phase voltages exhibit three voltage levels when the speed is lower than 2000 rpm, and five levels when the speed is higher than 2000 rpm. Phase voltages with CBCB-MPC are characterized by a more chaotic behaviour and exhibit the fifth level even in the low-speed working range. However, in both cases, phase voltages are characterized by $dv/dt$ at most equal to one HB DC link voltage over the entire working range. Voltage spectra with VVB-MPC present harmonics lower than 5% of the fundamental except when the speed is equal to 4000 rpm when the overmodulation region is reached. Concerning the CBCB-MPC, voltage spectra are characterized by higher harmonics amplitude almost in every considered working point, especially in the low-speed range where low-frequency harmonics reach 20% of the fundamental.

A comparison between instantaneous CMV trends is reported in Fig. 7(v-z): with respect to VVB-MPC, the CMVs maximum instantaneous value is equal to 18.33 V, except when the speed is equal to 4000 rpm where it is equal to 36.66 V; a much worse behaviour can be noted with the CBCB-MPC, where the most frequent peak value is equal to 55 V and the maximum peak value is equal to 110 V which occur in the low-speed range. This behaviour is emphasized in Fig. 8, where CMV instantaneous peak values over the defined working range are reported. It can be noted that the control goal of minimizing the CMV with the VVB-MPC, which is synthesized in Fig. 4b, has been reached over the entire defined working range, since the CMV peak is always equal to $v_{DC}/3$ (1.e. 18.33 V, when $v_{DC}$ = 55 V), except in WPs 1, 6, and 11, where the CMV peak reaches the value of $2v_{DC}/3$ equal to 36.66 V. This behaviour is justified by taking into account that only when the speed is equal to the rated value and the load is higher than half the rated torque, it is mandatory to employ the VVs $v_1$, $v_5$, $v_{27}$, $v_{35}$, $v_{57}$, and $v_{61}$ are employed where a higher CMV peak value cannot be avoided. On the other hand, no attention is paid to CMVs in the CBCB-MPC algorithm design. Only when the speed reaches the rated value, CMV behaviours become similar.

The phase currents in the time and frequency domain, when the CBCB-MPC and the VVB-MPC are adopted, are shown in Fig.9 (a-h) and Fig.9 (i-p), respectively, when the load torque is varied over the defined working range and the speed is constant and equal to 3000 rpm. Comparing CBCB-MPC and VVB-MPC current spectra, it can be noted that also, in this case, VVB-MPC guarantees a lower harmonic content over the entire working range, although the difference is less marked, if compared with voltage spectra: the worst case takes place when speed is equal to 200 rpm and the low-frequency harmonics reach the maximum value of 4% and 3 % when CBCB and VVB are considered, respectively.

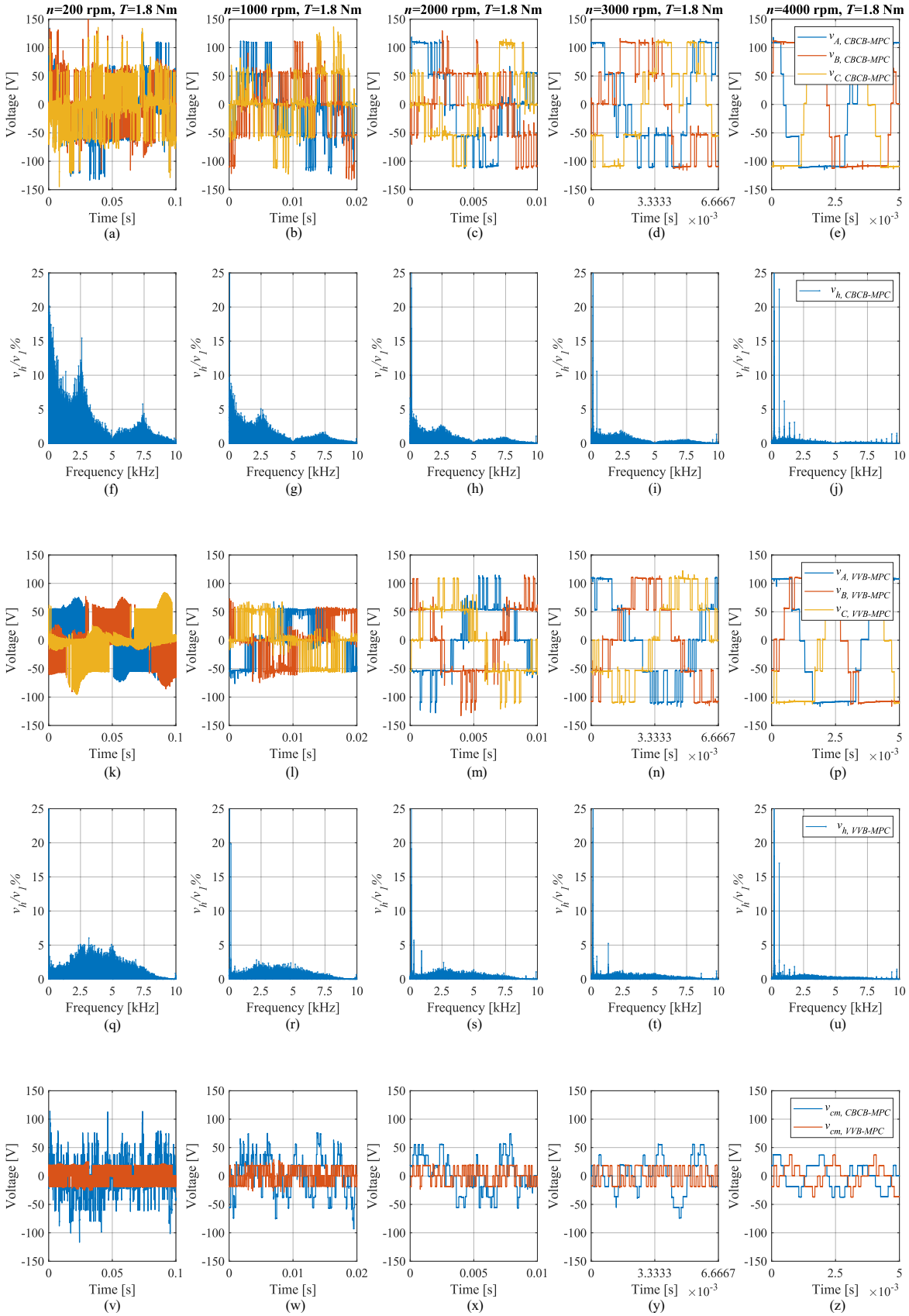


**Fig. 7.** Analysis for fixed load torque (1,8 Nm), varying the speed over the defined working range: (a-e) CBCB-MPC phase voltages, (f-j) CBCB-MPC phase voltage spectra, (k-p) VVB-MPC phase voltages, (q-u) VVB-MPC phase voltage spectra, (v-z) CBCB and VVB MPC common mode voltages comparison.

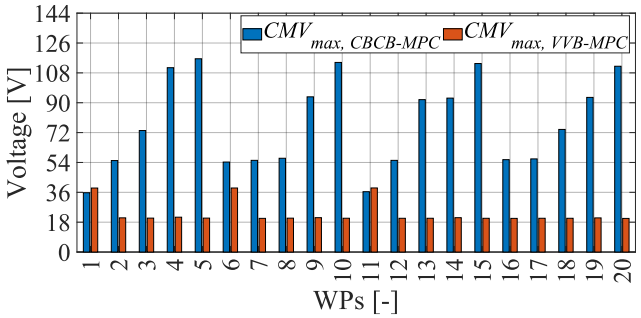


**Fig. 8.** Comparison between peak values of the common mode voltage in each working point with CBCB-MPC and VVB-MPC.

In Fig. 10 a half-period of the phase voltages expressed in p.u. and the GCSs related to the VVB-MPC are reported when the load torque is set to zero and the speed is 3000 rpm. It is easy to see that the GCS constraints are fulfilled, since only one or, at least, two GCSs change state over two adjacent sampling instants, according to Fig. 4(c). The apparent switching frequency $f_{sw}$ over the defined working range for the CBCB-MPC and the VVB-MPC are reported in Fig. 11(a) and in Fig. 11(e), respectively. Switching frequency estimation has been carried out by counting the phase voltage level transitions $N_t$ over the observation window and dividing by double the observation window $T_w$, according to (28):

$$f_{sw} = \frac{N_t}{2T_w} \tag{19}$$

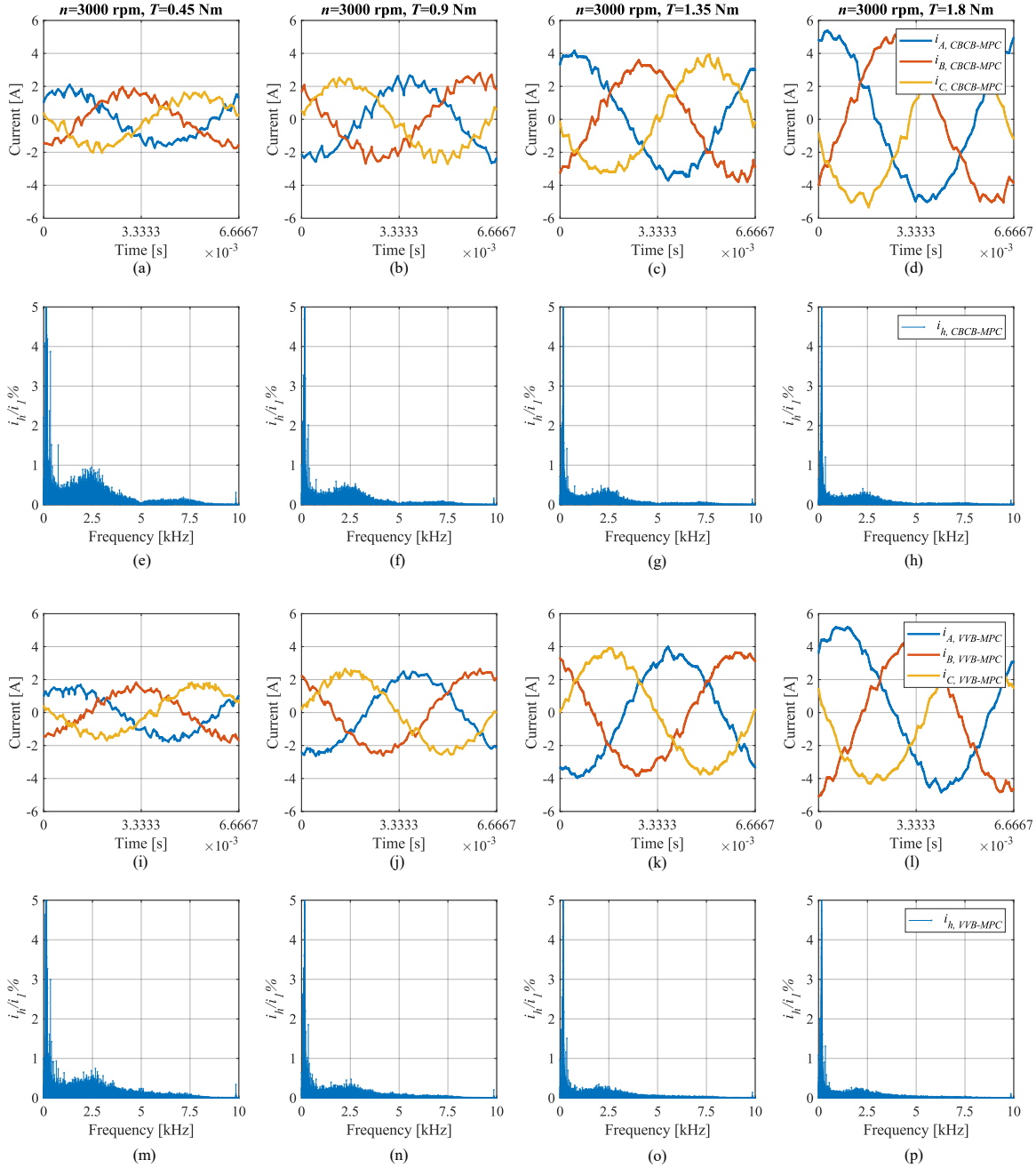


**Fig. 9.** Analysis for fixed speed (3000 rpm), varying the load torque over the defined working range: (a-d) CBCB-MPC phase currents, (e-h) CBCB-MPC phase current spectra, (i-l) VVB-MPC phase currents, (m-p) VVB-MPC phase current spectra.

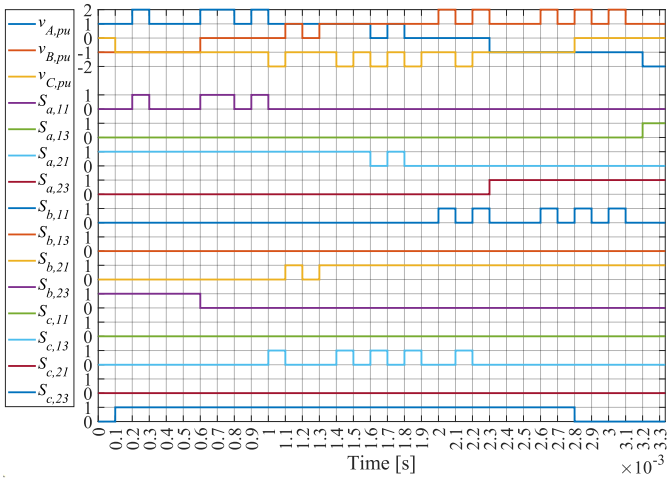


**Fig. 10.** Phase voltages and GCSs related to VVB-MPC, with speed equal to 3000 rpm at no load.

It can be noted that, in the considered working range, the apparent switching frequency varies from 1800 to 2600 Hz with an average apparent switching frequency equal to 2200 Hz when CBCB-MPC is adopted. Instead, the apparent switching frequency varies from 1400 to 1900 Hz with an average apparent switching frequency equal to 1700 Hz when VVB-MPC is adopted. It must be underlined that VVB-MPC guarantees at the same time a lower switching frequency and a better voltage and current harmonic content over the entire working range if compared to the CBCB-MPC. This behaviour is confirmed by the current and voltage THD maps over the adopted working range, reported in Fig. 11 (b-c) and Fig. 11 (f-g). In detail, it can be noted that the current THD varies in the range of 7-25% and 5-21% when CBCB-MPC and VVB-MPC are adopted, respectively. In both cases, for a fixed speed, the THD drastically decreases when the load torque increases. This behaviour is correlated with an increment of the fundamental frequency. Moreover, it can be noted a correlation between the current THD and the speed, such that the THD slowly increases when the speed increases. This behaviour can be justified by a progressive decrement in the switching frequency when the speed increases. About the voltage THD, it varies in the range of 40-300% and 30-200%, respectively. It can be noted that the THD variation is strictly correlated to the speed. In detail, when the speed increases, the THD decreases. Moreover, the voltage THD is quite independent of the load torque.

The CMV rms value over the defined working range is reported in Fig. 11(d) and Fig. 11(h), for CBCB and VVB-MPC, respectively. In detail, it can be noted that the CMV rms value over the defined working range is always quite low and the voltage variation over the working range is quite small, 12 – 18 V, when VVB-MPC is adopted. This analysis confirms that the goal of minimizing the common mode voltage with VVB-MPC has been fulfilled. Moreover, the CMV harmonic content results to be quite independent of the working range. Concerning CBCB-MPC, voltage variation over the working range is 22 – 32 V, thus, CMV rms values are higher than VVB-MPC over the entire working range, as was expected.

To investigate the electromagnetic torque trend and the torque ripple, the electromagnetic torque has been estimated starting by the control current in the *d-q* reference frame, according to the following relation:

$$T_{em} = \frac{3}{2} p \left[ \lambda_{PM} i_q - \left( L_q - L_d \right) i_d i_q \right] \tag{20}$$

A comparison between the electromagnetic torque trends generated with CBCB-MPC and VVB-MPC when the load torque varies over the defined range and when the speed is equal to 2000 and 3000 rpm is reported in Fig 12.

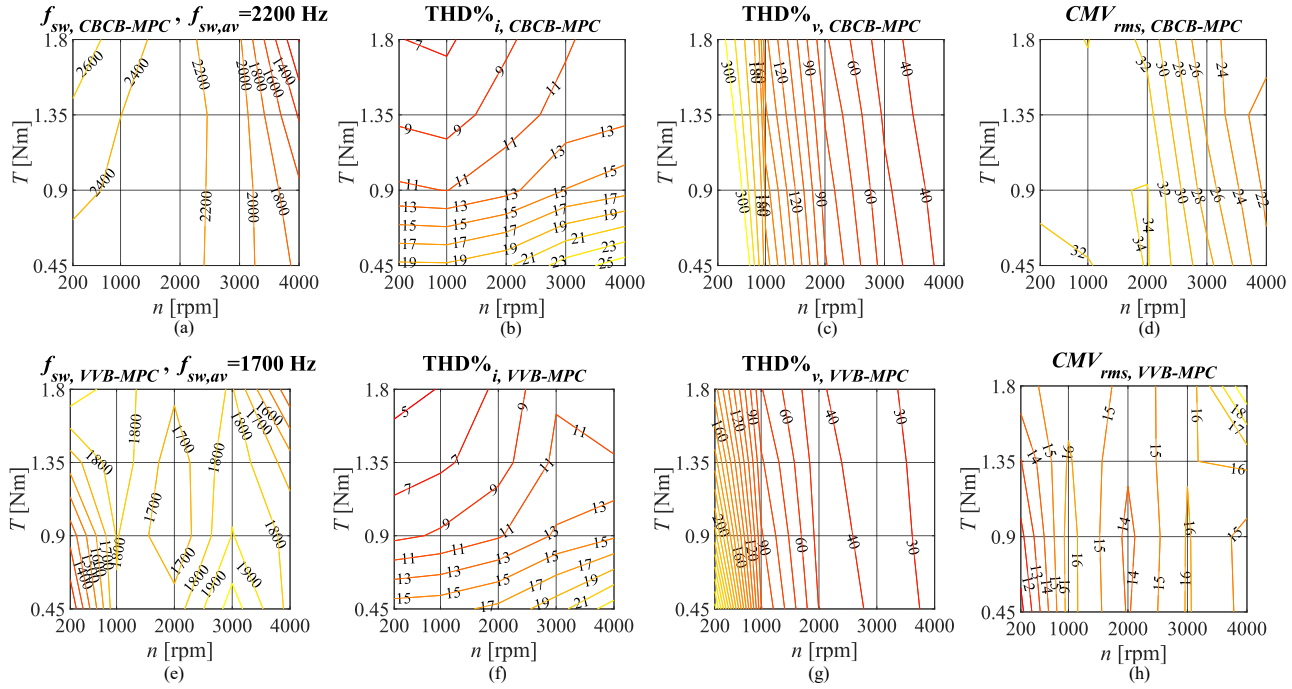


**Fig. 11.** Comparison tools: (a) CBCB-MPC apparent switching frequency, (b) CBCB-MPC current THD, (c) CBCB-MPC voltage THD, (d) CBCB-MPC CMV rms value, (e) VVB-MPC apparent switching frequency, (f) VVB-MPC current THD, (g) VVB-MPC voltage THD, (h) VVB-MPC CMV rms value.

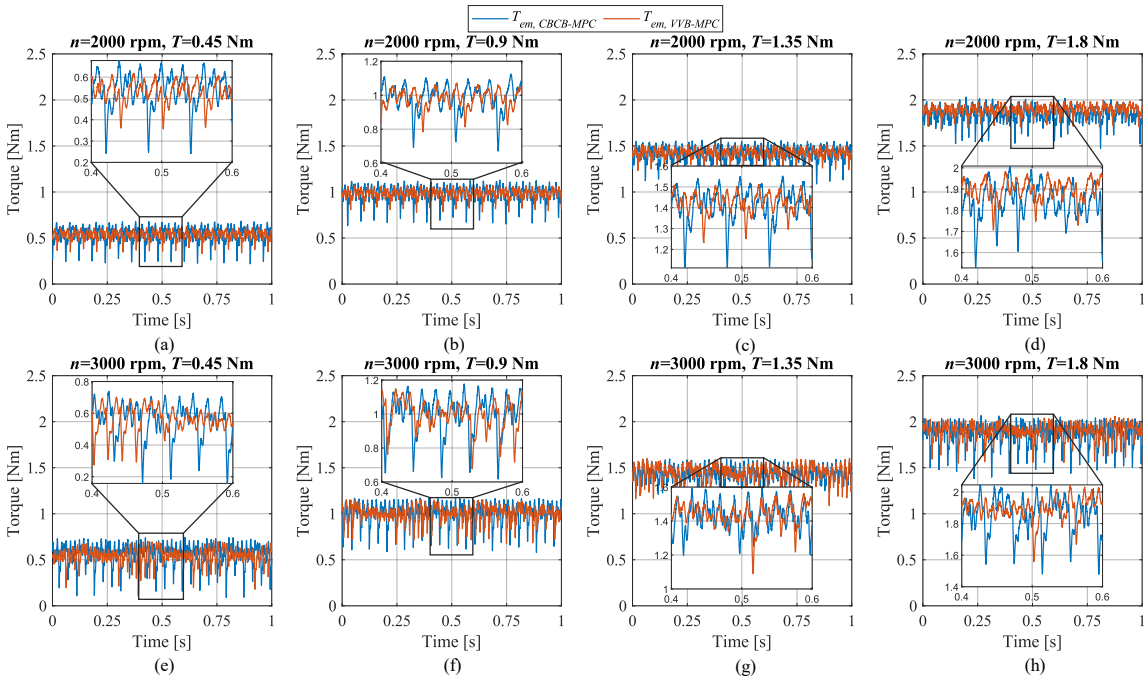


**Fig. 12.** Comparative analysis varying the load torque over the defined working range: (a-d) comparison at 2000 rpm, (e-h) comparison at 3000 rpm.

It can be noted that the VVB-MPC guarantees a lower torque ripple in every working condition, except when the speed is 3000 rpm and the torque is 1.35 Nm, where torque ripple values are comparable. To quantify the torque ripple over the entire defined working range, the torque ripple rms value, expressed in percent with respect to the average torque, has been adopted according to [28]:

$$\Delta T\%_{em} = \frac{100}{T_{em,avg}} \sqrt{\frac{1}{N_s} \sum_{k=1}^{N_s} \left( T_{em}(k) - T_{em,avg} \right)^2} \qquad (21)$$

where $N_s$ is the number of samples over the defined observation window and $T_{em,avg}$ is the average electromagnetic torque value. In Fig. 13 (a-b) the torque ripple maps over the defined working range with the two compared strategies are reported.

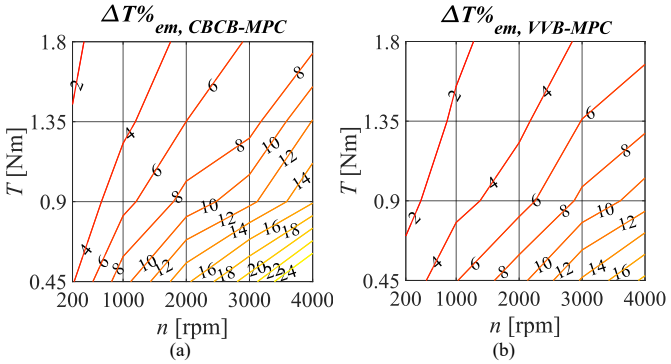


**Fig. 13.** Comparison tools: (a) CBCB-MPC torque ripple rms percentage values, (b) VVB-MPC torque ripple rms percentage values.

It can be noted that the torque ripple varies in the range of 2-24% and 1-16% when CBCB-MPC and VVB-MPC are adopted, respectively. In detail, both torque ripple map trends are very similar to the respective current THD% trends, such that there is a strong correlation with the motor speed. Also in this case, VVB-MPC guarantees a lower torque ripple over the entire working range.

### *C. Dynamic condition analysis*

In Fig. 14 a comparison between the electric drive dynamic behaviour obtained with the two compared strategies is reported. In detail, IPMSM phase voltages, phase currents, speed, and load torque trends during the whole dynamic cycle are reported in Fig. 14 (a) and (b), respectively. It is interesting to note that, in both cases, the currents reach the reference values in about 2 ms with a negligible overshoot. The speed transient ends in about 500 ms with about 200 rpm overshoot. The system exhibits also a good rejection of external disturbances, as can be seen when the load torque is applied and next removed. In detail, the speed transient due to the external disturbance ends in about 0.3 s. The reported trends state that both algorithms guarantee good dynamic performance, with a reduced speed and torque ripple. Thus no remarkable differences in the dynamic response have to be underlined.

## VI. Conclusions

In this work, the design and implementation of a novel multi-objective Voltage-Vector-Based FCS-MPC for PMSM drive fed by a 3P-5L CHBMI have been carried out. The control goals deal with computational burden minimization, CMVs minimization, GCSs transitions minimization, and phase voltages *dv/dt* minimization. The first goal is fulfilled by imposing that, at a certain sampling instant, future state prediction must be carried out by considering the set of adjacent VVs with respect to the currently applied VV. In this way, only 7 (instead of 4096) predictions must be carried out per sampling period. This constraint also allows for fulfilling the voltages *dv/dt* minimization.

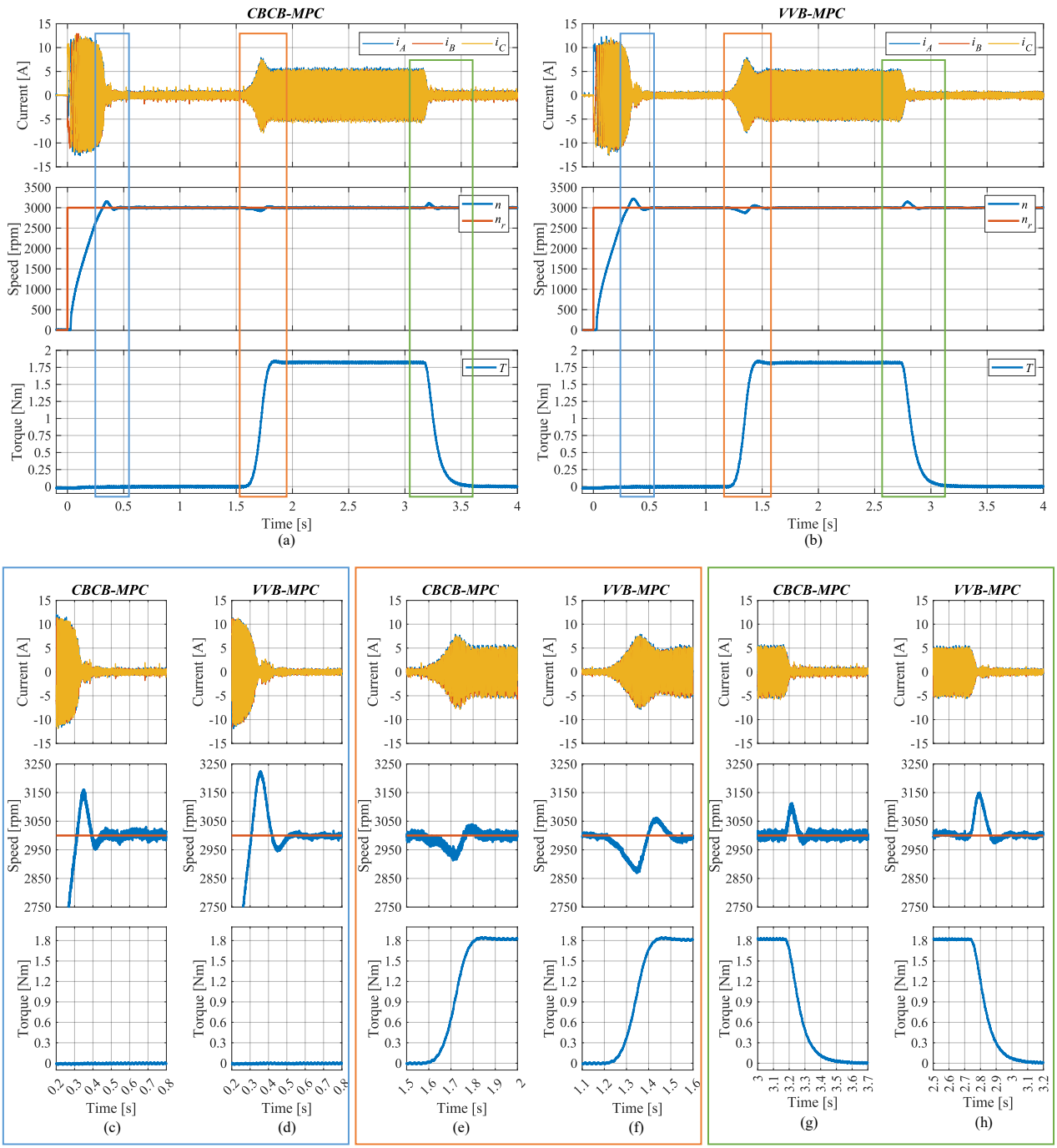


**Fig. 14.** Comparison between electric drive dynamic behaviour under a 0-3000 rpm acceleration and load torque variation: (a) CBCB-MPC, (b) VVB-MPC, (c-d) zoom on acceleration, (e-f) zoom on load torque application, (g-h) zoom on load torque exclusion.

The second goal is fulfilled by the elimination of redundant VVs which don't guarantee the minimum CMVs. The third goal is fulfilled by selecting GCSs such that only one or, at most, two, GCSs change state in a transition, i.e., only one or two HBs legs are changing state. These goals are reached through an offline optimization process. Thanks to the offline optimization procedure, the proposed online FCS-MPC algorithm does not require additional computation stages if compared to a non-constrained FCS-MPC. Indeed, the online VVs selection is carried out by acceding to LUTs; this operation doesn't affect the computational burden and the execution time. Moreover, the offline optimization process allows for reaching the proposed goals without synthesizing them into the cost function. Thus, no additional terms must be added to the cost function, with respect to a standard FCS-MPC and no weighting factors must be tuned. For control validation purposes, a detailed experimental comparative analysis with a CBCB-MPC strategy both in steady-state and dynamic working conditions has been carried out. Experimental results confirm that the proposed algorithm meets the proposed control goals and, at the same time, it guarantees better electric drive performance in steady-state working conditions in terms of voltage and current

harmonic content, voltage and current THD, switching frequency and torque ripple compared to the CBCB-MPC. Thus, the proposed strategy allows to reduce at the same time the switching frequency, which is correlated to the switching losses, and the torque ripple. The system dynamic behaviour is quite fast and the system is able to reject external disturbance and work in the defined set point. Comparison with the CBCB-MPC shows no sensitive difference in terms of dynamic performance.

## REFERENCES

[1] S. Kouro et al., "Recent Advances and Industrial Applications of Multilevel Converters," in *IEEE Transactions on Industrial Electronics*, vol. 57, no. 8, pp. 2553-2580, Aug. 2010.

[2] M. A. Perez, S. Ceballos, G. Konstantinou, J. Pou and R. P. Aguilera, "Modular Multilevel Converters: Recent Achievements and Challenges," in *IEEE Open Journal of the Industrial Electronics Society*, vol. 2, pp. 224-239, 2021.

[3] T. H. Nguyen, K. A. Hosani, M. S. E. Moursi and F. Blaabjerg, "An Overview of Modular Multilevel Converters in HVDC Transmission Systems With STATCOM Operation During Pole-to-Pole DC Short Circuits," in *IEEE Transactions on Power Electronics*, vol. 34, no. 5, pp. 4137-4160, May 2019.

[4] B. Singh, R. Kumar and P. Kant, "Adjustable Speed Induction Motor Drive Fed by 13-Level Cascaded Inverter and 54-Pulse Converter," in *IEEE Transactions on Industry Applications*, vol. 58, no. 1, pp. 890-900, Jan.-Feb. 2022.

[5] H. Abu-Rub, J. Holtz, J. Rodriguez and G. Baoming, "Medium-Voltage Multilevel Converters—State of the Art, Challenges, and Requirements in Industrial Applications," in *IEEE Transactions on Industrial Electronics*, vol. 57, no. 8, pp. 2581-2596, Aug. 2010.

[6] A. Poorfakhraei, M. Narimani and A. Emadi, "A Review of Multilevel Inverter Topologies in Electric Vehicles: Current Status and Future Trends," in *IEEE Open Journal of Power Electronics*, vol. 2, pp. 155-170, 2021.

[7] L. Liu, H. Li, S. -H. Hwang and J. -M. Kim, "An Energy-Efficient Motor Drive With Autonomous Power Regenerative Control System Based on Cascaded Multilevel Inverters and Segmented Energy Storage," in *IEEE Transactions on Industry Applications*, vol. 49, no. 1, pp. 178-188, Jan.-Feb. 2013.

[8] F. Chang, O. Ilina, M. Lienkamp and L. Voss, "Improving the Overall Efficiency of Automotive Inverters Using a Multilevel Converter Composed of Low Voltage Si mosfets," *in IEEE Transactions on Power Electronics*, vol. 34, no. 4, pp. 3586-3602, April 2019.

[9] S. Vazquez, J. Rodriguez, M. Rivera, L. G. Franquelo and M. Norambuena, "Model Predictive Control for Power Converters and Drives: Advances and Trends," in *IEEE Transactions on Industrial Electronics*, vol. 64, no. 2, pp. 935-947, Feb. 2017.

[10] P. Karamanakos, E. Liegmann, T. Geyer and R. Kennel, "Model Predictive Control of Power Electronic Systems: Methods, Results, and Challenges," in *IEEE Open Journal of Industry Applications*, vol. 1, pp. 95-114, 2020.

[11] P. Karamanakos and T. Geyer, "Guidelines for the Design of Finite Control Set Model Predictive Controllers," in *IEEE Transactions on Power Electronics*, vol. 35, no. 7, pp. 7434-7450, July 2020, doi: 10.1109/TPEL.2019.2954357.

[12] C. Qi, X. Chen, P. Tu and P. Wang, "Cell-by-Cell-Based Finite-Control-Set Model Predictive Control for a Single-Phase Cascaded H-Bridge Rectifier," in *IEEE Transactions on Power Electronics*, vol. 33, no. 2, pp. 1654-1665, Feb. 2018.

[13] T. He, M. Wu, R. P. Aguilera, D. D. -C. Lu, Q. Liu and S. Vazquez, "Low Computational Burden Model Predictive Control for Single-Phase Cascaded H-Bridge Converters Without Weighting Factor," in *IEEE Transactions on Industrial Electronics*, vol. 70, no. 3, pp. 2396-2406, March 2023.

[14] P. Karamanakos, K. Pavlou and S. Manias, "An Enumeration-Based Model Predictive Control Strategy for the Cascaded H-Bridge Multilevel Rectifier," in *IEEE Transactions on Industrial Electronics*, vol. 61, no. 7, pp. 3480-3489, July 2014.

[15] Y. Zhang, X. Wu, X. Yuan, Y. Wang and P. Dai, "Fast Model Predictive Control for Multilevel Cascaded H-Bridge STATCOM With Polynomial Computation Time," in *IEEE Transactions on Industrial Electronics*, vol. 63, no. 8, pp. 5231-5243, Aug. 2016.

[16] Y. Zhang, X. Wu and X. Yuan, "A Simplified Branch and Bound Approach for Model Predictive Control of Multilevel Cascaded H-Bridge STATCOM," in *IEEE Transactions on Industrial Electronics*, vol. 64, no. 10, pp. 7634-7644, Oct. 2017.

[17] Q. Xiao et al., "Modulated Model Predictive Control for Multilevel Cascaded H-Bridge Converter-Based Static Synchronous Compensator," in *IEEE Transactions on Industrial Electronics*, vol. 69, no. 2, pp. 1091-1102, Feb. 2022.

[18] P. Cortés, A. Wilson, S. Kouro, J. Rodriguez and H. Abu-Rub, "Model Predictive Control of Multilevel Cascaded H-Bridge Inverters," in *IEEE Transactions on Industrial Electronics*, vol. 57, no. 8, pp. 2691-2699, Aug. 2010.

[19] M. Chen, D. Niu, L. Zhang and X. Liu, "Common-Mode Voltage Elimination of Multilevel Converters With Reduced Switching Loss Using Sawtooth-Carrier-Based PWM," in *IEEE Transactions on Power Electronics*, vol. 38, no. 10, pp. 12024-12034, Oct. 2023.

[20] C. Xiong, H. Xu, C. Fang and H. Zhang, "Model predictive control method to reduce common-mode voltage for permanent-magnet synchronous machine drives," 2017 IEEE Transportation Electrification Conference and Expo, Asia-Pacific (ITEC Asia-Pacific), Harbin, China, 2017, pp. 1-6.

[21] M. L. Parvathy and T. V. Kumar, "An Enhanced Predictive Current Control Scheme for Common Mode Voltage Alleviation and Improvement of Torque Response of PMSM Drive," in *IEEE Journal of Emerging and Selected Topics in Power Electronics*, vol. 11, no. 2, pp. 2139-2150, April 2023.

[22] L. Guo, X. Zhang, S. Yang, Z. Xie and R. Cao, "A Model Predictive Control-Based Common-Mode Voltage Suppression Strategy for Voltage-Source Inverter," in *IEEE Transactions on Industrial Electronics*, vol. 63, no. 10, pp. 6115-6125, Oct. 2016.

[23] H. Niu, Z. Ma, Y. Han, G. Chen, Z. Liao and G. Lin, "Model Predictive Control with Common-Mode Voltage Minimization for a Three-level NPC Inverter PMLSM Drive System," 2021 13th International Symposium on Linear Drives for Industry Applications (LDIA), Wuhan, China, 2021, pp. 1-5.

[24] X. Wang, X. Fang, S. Lin, F. Lin and Z. Yang, "Predictive Common-Mode Voltage Suppression Method Based on Current Ripple for Permanent Magnet Synchronous Motors," in *IEEE Journal of Emerging and Selected Topics in Power Electronics*, vol. 7, no. 2, pp. 946-955, June 2019.

[25] P. Cortes, J. Rodriguez, C. Silva and A. Flores, "Delay Compensation in Model Predictive Current Control of a Three-Phase Inverter," in *IEEE Transactions on Industrial Electronics*, vol. 59, no. 2, pp. 1323-1325, Feb. 2012.

[26] A. O. Di Tommaso et al., "A Simple Software-based Resolver To Digital Conversion System," IECON 2022 – 48th Annual Conference of the IEEE Industrial Electronics Society, Brussels, Belgium, 2022, pp. 1-6.

[27] A. O. D. Tommaso et al., "Field Oriented Control of IPMSM Fed by Multilevel Cascaded H-Bridges Inverter with NI-SOM sbRIO-9651 FPGA controller," 2022 International Symposium on Power Electronics, Electrical Drives, Automation and Motion (SPEEDAM), Sorrento, Italy, 2022, pp. 88-93.

[28] M. J. Navardi, J. Milimonfared and H. A. Talebi, "Torque and Flux Ripples Minimization of Permanent Magnet Synchronous Motor by a Predictive-Based Hybrid Direct Torque Control," in *IEEE Journal of Emerging and Selected Topics in Power Electronics*, vol. 6, no. 4, pp. 1662-1670, Dec. 2018.